

Self-Refining Training for Amortized Density Functional Theory

Majdi Hassan* ^{1,2}Cristian Gabellini ³Hatem Helal ³Dominique Beaini ^{1,2,3}Kirill Neklyudov ^{1,2}¹Université de Montréal ²Mila - Quebec AI Institute ³Valence Labs

Abstract

Density Functional Theory (DFT) allows for predicting all the chemical and physical properties of molecular systems from first principles by finding an approximate solution to the many-body Schrödinger equation. However, the cost of these predictions becomes infeasible when increasing the scale of the energy evaluations, e.g., when calculating the ground-state energy for simulating molecular dynamics. Recent works have demonstrated that, for substantially large datasets of molecular conformations, Deep Learning-based models can predict the outputs of the classical DFT solvers by amortizing the corresponding optimization problems. In this paper, we propose a novel method that reduces the dependency of amortized DFT solvers on large pre-collected datasets by introducing a self-refining training strategy. Namely, we propose an efficient method that simultaneously trains a deep-learning model to predict the DFT outputs and samples molecular conformations that are used as training data for the model. We derive our method as a minimization of the variational upper bound on the KL-divergence measuring the discrepancy between the generated samples and the target Boltzmann distribution defined by the ground state energy. To demonstrate the utility of the proposed scheme, we perform an extensive empirical study comparing it with the models trained on the pre-collected datasets. Finally, we open-source our implementation of the proposed algorithm, optimized with asynchronous training and sampling stages, which enables simultaneous sampling and training. Code is available at <https://github.com/majhas/self-refining-dft>.

1 Introduction

Density Functional Theory (DFT) is a quantum-mechanical approximation for solving the electronic structure problem (Hohenberg and Kohn, 1964a; Kohn and Sham, 1965a; Roothaan, 1951), commonly used in drug design, materials discovery, and the characterization of chemical properties (Pribram-Jones et al., 2015). Among various computational methods, DFT is favored for its balance of accuracy and scalability (Keith et al., 2021). However, conventional DFT solvers usually focus on a single Hamiltonian, i.e. single geometry of the given molecule (Parr, 1980). This naturally makes them unsuitable for tasks that require sequentially evaluating energy across multiple configurations, such as conformational sampling, transition path sampling, and molecular dynamics (Leimkuhler and Matthews, 2015). In these tasks, for every generated geometry, one has to re-run DFT computations from scratch to find the electron density that minimizes the total energy (Payne et al., 1992).

*Correspondence: majdi.mhas@gmail.com (Majdi Hassan)

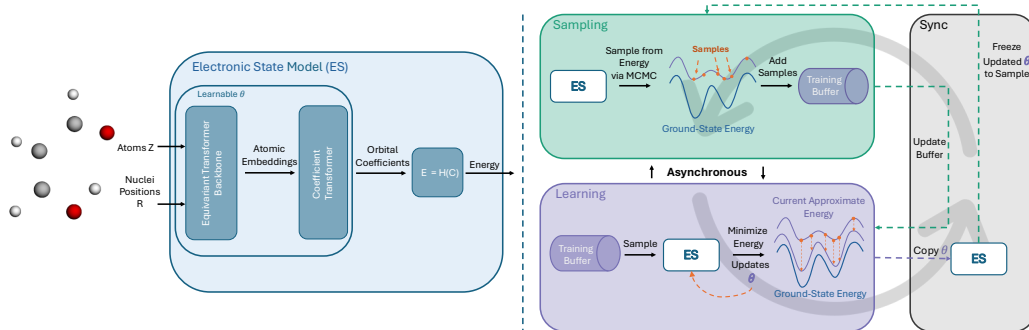


Figure 1: Overview of the self-refining training. From atom types Z and positions R , the electronic state model predicts orbital coefficients which are used to compute the energy. Self-Refining Training operates in two asynchronous phases: (1) **sampling** conformations under the current energy estimation, and (2) **energy minimization** of the sampled conformations updates the model parameters θ . A synchronization step periodically updates the parameters of the sampler with the latest parameters from the **energy minimization** phase.

In contrast, deep learning (DL) is a promising approach to scaling DFT-based computations, e.g. predicting energies to near quantum-chemical accuracy or determining the converged Hamiltonian matrix. In general, deep learning methods offer excellent scalability and generalizability, provided sufficiently large, high-quality datasets are available (Deng et al., 2009; Beaini et al., 2023). Yet, the creation of these datasets presents a major bottleneck because the labeling process involves running the conventional DFT methods (e.g. self-consistent field (SCF) method (Roothaan, 1951)) for each data point. This process makes data generation prohibitively expensive at large scales. For instance, it took *two years* to generate 3.8 million conformations for the PCQ dataset (Nakata and Shimazaki, 2017).

Recent work (Zhang et al., 2024a; Mathiasen et al., 2024; Li et al., 2024) has taken a step toward overcoming this data-labeling burden by proposing a different training scheme. Namely, instead of predicting the energy, they predict the electronic state and define *implicit DFT loss* as the energy of the predicted electronic state, which amounts to a single iteration of SCF compared to a hundred required for labeling. We call this family of models as electronic state (ES) models. This approach demonstrated comparable accuracy to prior work (Schütt et al., 2019; Unke et al., 2021; Yu et al., 2023) while avoiding the dependency on data labeling. In our approach, we push this idea further by reducing the need for pre-generating the molecular conformations themselves, thus enabling the self-refining training of the ES model where we simultaneously train the electronic state model to minimize the energy via the implicit DFT loss and sample conformations to be used as training data.

Main contributions. We propose a framework for learning the electronic state model that accurately predicts DFT outputs while significantly reducing the reliance on pre-collected data. The key idea is that the data generation and the energy estimation steps are complementary problems to each other, i.e. a partial solution of one step enhances the performance of another, creating a virtuous cycle. Thus, one can use the current (in the process of training) ES model to generate new samples (**sampling** step), which are then used for further training of the ES model (**energy minimization** step). The proposed framework rests on the fact that the minimum of the predicted electronic state energy has to be achieved *point-wise* which allows for a great flexibility in the choice of the distribution of samples. We formalize this insight by deriving a variational upper bound on the KL-divergence between the distribution of samples and the target Boltzmann distribution of the ground-state energy. Furthermore, we demonstrate that the Wasserstein gradient (Ambrosio and Savaré, 2007) of the derived upper bound corresponds to the Langevin dynamics, which motivates its usage for generating new samples.

We empirically compare our method with the baselines and demonstrate that it achieves better performance on the test-set when using the same amount of the training data and superior performance on samples using the overdamped molecular dynamics. These properties are especially interesting in the data-scarce scenarios, which we highlight by achieving chemical accuracy using as few as 25 conformations. Lastly, we provide an open-source implementation of our method that allows for efficient asynchronous training.

2 Background

2.1 The Schrödinger Equation

Quantum mechanics offers a complete theory for predicting all the chemical and physical properties of atomic systems through the solution of the stationary Schrödinger equation. Namely, for the given

Hamiltonian operator \hat{H} acting on the wavefunctions $\psi(r_1, \dots, r_n) : \mathbb{R}^{3n} \rightarrow \mathbb{C}$ of n electrons at positions r_1, \dots, r_n , one has to find all the eigenvalues E_i and the corresponding eigenstates ψ_i , i.e.

$$\hat{H}\psi_i(r_1, \dots, r_n) = E_i\psi_i(r_1, \dots, r_n). \quad (1)$$

For molecule with nuclei at positions R and atomic charges Z , the Hamiltonian operator is

$$\hat{H} = -\frac{1}{2} \sum_{i=1}^n \nabla_i^2 + \sum_{i < j} \frac{1}{\|r_i - r_j\|} - \sum_{i,I} \frac{Z_I}{\|r_i - R_I\|} + \sum_{I < J} \frac{Z_I Z_J}{\|R_I - R_J\|}, \quad (2)$$

where $\nabla_i^2 \psi = \langle \nabla_i, \nabla_i \psi \rangle$ and ∇_i is the gradient w.r.t. the position r_i of the i -th electron. This is the so-called Born-Oppenheimer approximation where the positions of the nuclei R are fixed input parameters of Hamiltonian and the operator acts on wavefunctions ψ which define electronic states and have to respect the fermionic anti-symmetry, i.e. $\psi(r_i, \dots, r_j) = -\psi(r_j, \dots, r_i)$

For many applications, the eigenstate ψ_0 (*the ground state*) corresponding to the lowest eigenvalue E_0 (the lowest energy) is of a particular interest. Alternatively to Eq. (1), this state can be defined as the solution of the following variational problem

$$E_0 = \min_{\psi} \frac{\langle \psi, \hat{H} \psi \rangle}{\langle \psi, \psi \rangle}, \quad \langle \psi, \xi \rangle := \int dr_1, \dots, dr_n \psi^*(r_1, \dots, r_n) \xi(r_1, \dots, r_n), \quad (3)$$

where ψ^* is the complex conjugate of ψ . Finding $\psi_0(r_1, \dots, r_n)$ by directly minimizing the energy is an extremely challenging computational problem because it requires solving the optimization problem w.r.t. high-dimensional functions $\psi : \mathbb{R}^{3n} \rightarrow \mathbb{C}$.

2.2 Density Functional Theory

As an attempt to avoid the optimization in the space of high-dimensional wavefunctions Hohenberg and Kohn (1964b) established Density Functional Theory (DFT), which proposes an alternative formulation to the variational problem in Eq. (3). Namely, instead of the optimization in the space of wavefunctions ($\psi : \mathbb{R}^{3n} \rightarrow \mathbb{C}$), one can minimize energy w.r.t. the electronic density ($\rho : \mathbb{R}^3 \rightarrow \mathbb{R}$)

$$E_0 = \min_{\psi} \frac{\langle \psi, \hat{H} \psi \rangle}{\langle \psi, \psi \rangle} = \min_{\rho} F[\rho] + V[\rho], \quad \rho(r) = \int dr_2 \dots dr_n |\psi(r, r_2, \dots, r_n)|^2, \quad (4)$$

where $\rho(r)$ is the normalized electronic density (i.e. $\int dr \rho(r) = n$), $F[\rho]$ is the universal density functional represented by the parts of the Hamiltonian that do not depend on R , and $V[\rho]$ is the system-dependent functional that is defined by nuclei positions R . However, the analytic form of the universal functional $F[\rho]$ is unknown and its efficient approximation is the main challenge in DFT.

The next conceptual leap forward was made by “simulating” many-body electron interactions via the effective one-electron potential (Kohn and Sham, 1965b), which allowed for reducing the problem of n interacting electrons to n independent one-electron problems. The latter can be efficiently solved under the Hartree-Fock family of the wavefunctions (Roothaan, 1951). Namely, one can parameterize the wavefunction using the orthonormal set of molecular orbitals ψ_i as follows

$$\psi(r_1, \dots, r_n) = \det[\Psi_{HF}], \quad (\Psi_{HF})_{ij} = \psi_i(r_j), \quad \langle \psi_i, \psi_j \rangle = \delta_{ij}. \quad (5)$$

Parameterizing the wavefunction as the determinant of Ψ_{HF} guarantees the fermionic anti-symmetry.

Linear Combination of Atomic Orbitals (LCAO) is a common approach for parameterizing molecular orbitals $\psi_i(r)$. Namely, each single-particle wavefunction is expanded in a predefined basis set, typically localized around atomic centers $\psi_i(r) = \sum_{\mu} c_{\mu i} \phi_{\mu}(r - R_{\mu})$, where $c_{\mu i}$ are the coefficients of $\psi_i(r)$ in the new basis $\phi_{\mu}(r - R_{\mu})$ (Hehre et al., 1969). Variational problem in Eq. (4) becomes

$$E_0 = \min_C E(C), \quad \text{subject to } C^{\dagger} S C = \mathbb{1}, \quad S_{\mu\nu} = \int dr \phi_{\mu}^*(r - R_{\mu}) \phi_{\nu}(r - R_{\nu}), \quad (6)$$

where C is the matrix of coefficients $c_{\mu i}$ in the new basis, $E(C)$ is the energy functional in this basis, and $C^{\dagger} S C = \mathbb{1}$ is the orthonormality condition of the orbitals ψ_i . Significant progress has already been made in the design of the effective potential and the basis set. That is why, throughout the paper, we assume that given the nuclei positions R we know the analytic form of the energy functional $E(C)$ and the overlap matrix S .

Algorithm 1: Self-Refining Training pseudocode (for **sampling** and **energy minimization**)

Input : Parametric model f_θ for which $f_\theta(R)^\dagger S(R) f_\theta(R) = \mathbb{1}$, the energy functional $E(R, C)$.
while not converged do
 Sample $R \sim q_\theta(R) \propto \exp(-E(R, f_\theta(R)))$ // using Monte Carlo methods
 Update f_θ by minimizing $\mathbb{E}_{q(R)}[E(R, f_\theta(R))]$ // using the collected samples R
return θ

3 Self-Refining Training for Amortized DFT

In this section, we present our method that simultaneously learns the DFT-based energy model of molecular conformations and samples these conformations from the Boltzmann distribution of the learned energy model. The foundation of our method is the variational upper bound on the KL-divergence between generated samples and the true Boltzmann density of molecular conformations which we derive in Section 3.1. Minimization of this upper bound w.r.t. the parameterized electronic state model corresponds to minimization of the predicted ground state energy on the samples (see Section 3.2). Whereas the minimization of the upper bound w.r.t. the distribution of the samples results in sampling from the Boltzmann density corresponding to the *parameterized* energy model (see Section 3.3). Building on these results, we propose Self-Refining Training algorithm in Section 3.4.

3.1 Variational Energy Bound

Deep Learning allows for an efficient amortization of the optimization problem from Eq. (6) over different molecular geometries defined by the nuclei positions R (Zhang et al., 2024a; Mathiasen et al., 2024). Indeed, making the energy functional $E(C)$ and the overlap matrix S explicitly dependent on R , one can define the energy model $E_0(R)$ as follows

$$E_0(R) = \min_C E(R, C), \text{ subject to } C^\dagger S(R) C = \mathbb{1}. \quad (7)$$

However, instead of directly modeling $E_0(R)$, we define *the electronic state model* as the solution of the following optimization problem

$$f^*(R) = \arg \min_{C: C^\dagger S(R) C = \mathbb{1}} E(R, C), \text{ which defines the energy model } E_0(R) = E(R, f^*(R)). \quad (8)$$

The target distribution of molecular conformations is defined by the following Boltzmann distribution

$$p^*(R) = \frac{1}{Z^*} \exp(-E(R, f^*(R))), \quad Z^* = \int dR \exp(-E(R, f^*(R))). \quad (9)$$

However, in practice, we have access neither to the density $p^*(R)$ nor to the samples from this density. The only supervision signal we have is the functional $E(R, C)$ from the optimization problem in Eq. (7), which defines the energy. In order to collect samples from $p^*(R)$ and learn its density model, we derive a practical upper bound on the KL-divergence between any density $q(R)$ and $p^*(R)$ in the following proposition.

Proposition 1. [Variational Energy Bound] *For any density $q(R)$, the KL-divergence between $q(R)$ and the ground-state Boltzmann distribution $p^*(R) \propto \exp(-E(R, f^*(R)))$ admits the following variational upper bound*

$$D_{\text{KL}}(q, p^*) \leq \underbrace{\mathbb{E}_{q(R)} \log q(R) + \mathbb{E}_{q(R)} E(R, f_\theta(R))}_{:= \Phi[q, f_\theta]} + \log Z^*, \quad (10)$$

where f_θ is a parametric approximation of f^ , which satisfies $f_\theta(R)^\dagger S(R) f_\theta(R) = \mathbb{1}$. For any $q(R)$, the bound becomes tight when $f_\theta(R) = f^*(R)$.*

See Appendix A.1 for the proof.

Both steps of our algorithm can be described as minimization of the upper bound in Proposition 1: the **sampling** step corresponds to the minimization of $\Phi[q, f_\theta]$ w.r.t. the distribution of samples

$q(R)$ and the **energy minimization** step corresponds to the minimization of $\Phi[q, f_\theta]$ w.r.t. the parameters of the electronic state model θ . In Alg. 1, we provide pseudocode for both steps in the most general form. Notably, these steps can be run asynchronously with periodic synchronization for exchanging the newly generated samples and current parameters of the electronic state model.

3.2 Energy Minimization

The **energy minimization** step corresponds to the learning the electronic state model $f_\theta(R)$ by minimization of the upper bound from Proposition 1. This can be done by minimizing $\Phi[q, f_\theta]$ w.r.t. the parameters of the model θ . However, first, we have to parameterize f_θ that satisfies the orthonormality conditions $f_\theta(R)^\dagger S(R) f_\theta(R) = \mathbb{1}$. To handle this constraint, we follow Head-Gordon and Pople (1988); Kasim et al. (2022); Li et al. (2023) and define the electronic state model as

$$f_\theta(R) = U\Lambda^{-1/2}U^T Q_\theta(R), \quad Q_\theta(R) = \text{Orthogonal}(\text{NN}_\theta(R)), \quad (11)$$

where $S(R) = U\Lambda U^T$, U and Λ are the corresponding matrices of eigenvectors and eigenvalues of $S(R)$, $\text{NN}_\theta(R)$ is the neural network output for the input coordinates R , and Orthogonal is any orthogonalization transformation, e.g. the QR-decomposition or the Cayley transform (in practice, we use the QR-decomposition). Thus, by straightforward calculations we have $f_\theta(R)^\dagger S(R) f_\theta(R) = \mathbb{1}$.

The minimization of the upper bound $\Phi[q, f_\theta] + \log Z^*$ boils down to the minimization of the energy model $E(R, f_\theta(R))$ on the samples from $q(R)$. We formalize this in the following statement, which is a straightforward corollary of Proposition 1.

Corollary 1. [Energy Minimization] *For any density $q(R)$ which is positive $q(R) > 0$ for the states with finite energies $\forall R : E(R, f^*(R)) < \infty$ except for sets of zero measure, we have*

$$f^* = \arg \min_{f_\theta} \Phi[q, f_\theta] = \arg \min_{f_\theta} \mathbb{E}_{q(R)} E(R, f_\theta(R)). \quad (12)$$

The practical value of this corollary is that the optimization of the electronic state model f_θ does not require any labeled data like ground truth energies or precalculated solutions of the optimization problem Eq. (7). This makes our framework independent of expensive dataset collection, analogously to the recent works by Zhang et al. (2024a); Mathiasen et al. (2024); Li et al. (2024). Indeed, the objective in Eq. (12) can be efficiently optimized using gradient-based approaches (we provide pseudocode in Alg. 2).

3.3 Sampling

Optimization of the upper bound from Proposition 1 w.r.t. the distribution $q(R)$ results in the **sampling** step. Namely, for the fixed parameteric model $f_\theta(R)$, in the following corollary we find the distribution $q(R)$ that minimizes $\Phi[q, f_\theta]$.

Corollary 2. [Sampling] *For any electronic state model $f_\theta(R)$, the optimum of the upper bound $\Phi[q, f_\theta]$ w.r.t. the density $q(R)$ is the Boltzmann distribution defined by the model $f_\theta(R)$, i.e.*

$$q^*(R) = \arg \min_q \Phi[q, f_\theta] = \frac{1}{Z_\theta} \exp(-E(R, f_\theta(R))). \quad (13)$$

See Appendix A.2 for proof. This result suggests that given the current approximation of the electronic state model f_θ the best distribution $q(R)$ we can get is the Boltzmann distribution corresponding to the current energy model $E(R, f_\theta(R))$.

Reducing the problem to sampling from the unnormalized density opens the door to a rich field of Monte Carlo methods, among which we choose the Langevin dynamics, which is motivated by the variational bound proposed in Proposition 1. Indeed, sampling from the Boltzmann density from Eq. (13) is different from the classical sampling problems because it happens in parallel to the updates of the parameters θ and the density itself. In this context, tuning an algorithm or training a model to sample from the target density might be wasteful if the density changes too quickly.

Instead, we assume that at every iteration the distribution $q(R)$ is reasonably close to the target $\exp(-E(R, f_\theta(R)))$. Therefore, we need to make several updates of $q(R)$ that minimize the bound

Algorithm 2: Self-Refining Training Algorithm

Input : Electronic state model f_θ , energy functional $E(R, C)$, replay buffer \mathcal{B} , length of the sampling chain T , step size dt , initial distribution of samples $p_0(R)$ and probability P

while *not converged* **do**

- Sample from current approximate of energy $E(R, f_\theta(R))$
- $R_0 \sim \mathcal{B}$ with prob. P or $R_0 \sim p_0(R)$ with prob. $(1 - P)$ // sample initial point
- for** $t = 0, \dots, T - dt$ **do**
 - $R_{t+dt} \leftarrow R_t - \nabla_R E(R_t, f_\theta(R_t))dt + \sqrt{2}dW_t$ // Langevin dynamics
 - $\mathcal{B} \leftarrow \mathcal{B} \cup R_T$ // update the buffer \mathcal{B}
 - Update electronic state model using samples from \mathcal{B}
- $\text{grad}_\theta \leftarrow \nabla_\theta \mathbb{E}_{R \sim \mathcal{B}} E(R, f_\theta(R))$ // estimate the gradient using samples from \mathcal{B}
- $\theta \leftarrow \text{Optimizer}(\theta, \text{grad}_\theta)$ // minimize the energy using the gradient

return θ

$\Phi[q, f_\theta]$. This can be formalized as following the negative gradient of $\Phi[q, f_\theta]$ w.r.t. the density $q(R)$. The natural choice for the gradient in the space of distribution is the Wasserstein gradient (Ambrosio and Savaré, 2007) since it can be efficiently implemented on the sample-level as transporting the samples along a vector field. We derive the Wasserstein gradient dynamics minimizing $\Phi[q, f_\theta]$ in the following proposition.

Proposition 2. [Wasserstein Gradient] *For the functional $\Phi[q, f_\theta]$ defined in Proposition 1, the gradient descent w.r.t. $q(R)$ corresponds to the following PDE*

$$\frac{\partial q_t(R)}{\partial t} = -\langle \nabla_R q_t(R) (-\nabla_R E(R, f_\theta(R))) \rangle + \Delta_R q_t(R), \quad (14)$$

which can be efficiently simulated via the following Stochastic Differential Equation (SDE)

$$dR_t = -\nabla_R E(R_t, f_\theta(R_t))dt + \sqrt{2}dW_t, \quad (15)$$

where W_t is the standard Wiener process.

For the proof see Appendix A.3. This results suggests generating new samples via the Langevin dynamics whereas the gradient $\nabla_R E(R_t, f_\theta(R_t))$ can be efficiently calculated by backpropagation (see Alg. 2 for the pseudocode).

3.4 Self-Refining Training Algorithm

The **energy minimization** and **sampling** steps together result in the Self-Refining Training algorithm, which we describe in Alg. 2. The essential part of the algorithm that allows for self-refinement is the energy functional $E(R, C)$ that provides the supervision signal in every point of the space R, C . This is similar but not identical to adversarial training (Goodfellow et al., 2014b) where only small perturbations of the training data are allowed, otherwise one has to re-label the generated sample. Furthermore, training on the samples from the Langevin dynamics aligns with the downstream applications of the learned energy model since it corresponds to the overdamped molecular dynamics.

In theory, Self-Refining Training does not require any pre-collected data, but, in practice, we find that pre-training the ES model $f_\theta(R)$ even on a small number of conformations provides a better initialization for further training. Additionally, for the initial distribution $p_0(R)$ of the Langevin dynamics we use the conformations from either the replay buffer or from the dataset. This provides the model with both “clean” and “noisy” samples for the learning stage, which improves the model’s ability to generalize as we will demonstrate later in the experiments section. Further details can be found in Appendix C.2.

Table 1: Performance across metrics for self-refining training in the *data-scarce* (10% of the available data) against a model with access to the full dataset (MD17 Hamiltonian). The ES + I-DFT is a model trained on pre-collected conformations, but using implicit DFT loss. ES + SR is a model trained with self-refining training. $\mathcal{D}_{X\%}$ means the model was trained using Self-Refinement and X% of pre-collected data. The evaluations were done on the test split of conformations of each molecule from MD17. We also include regression-based models to provide a comparison to the I-DFT loss objective.

Molecule Setting		$E[\mu E_h]$	$\mathbf{H}[\mu E_h] \downarrow$	$\epsilon[\mu E_h] \downarrow$	$\epsilon_{\text{HOMO}}[\mu E_h] \downarrow$	$\epsilon_{\text{LUMO}}[\mu E_h] \downarrow$	$\epsilon_{\Delta}[\mu E_h] \downarrow$
Ethanol	I-DFT + $\mathcal{D}_{100\%}$	63.33	91.01	413.25	489.96	1792.90	1341.80
	I-DFT + SR + $\mathcal{D}_{10\%}$	135.94	117.23	397.89	432.88	1567.50	1205.20
	I-DFT + SR + $\mathcal{D}_{100\%}$	83.84	86.36	291.74	336.17	1389.40	1090.90
Malondi-aldehyde	I-DFT + $\mathcal{D}_{100\%}$	773.00	165.30	655.20	622.00	3042.00	2679.00
	I-DFT + SR + $\mathcal{D}_{10\%}$	7089.00	555.50	2007.00	1834.00	7275.00	6219.00
	I-DFT + SR + $\mathcal{D}_{100\%}$	5411.00	527.00	1735.00	1682.00	6338.00	5284.00
Uracil	I-DFT + $\mathcal{D}_{100\%}$	49.24	47.05	366.78	231.44	1082.40	1146.10
	I-DFT + SR + $\mathcal{D}_{10\%}$	40.91	35.61	220.97	149.91	625.02	660.45
	I-DFT + SR + $\mathcal{D}_{100\%}$	38.34	33.64	205.14	142.99	694.23	748.30

Asynchronous Training. Crucially, our algorithm allows for asynchronous implementation of [energy minimization](#) and [sampling](#) steps. Indeed, both steps minimize the variational lower bound and their iterations resemble the coordinate descent w.r.t. different arguments of $E(R, C)$ (unlike adversarial networks (Goodfellow et al., 2014a)). Thus, one can generate new samples and update ES model parameters independently on different sets of GPUs. In particular, samples generated by the sampling process go into a temporary buffer, which, once full, triggers a synchronization step. During this step, the new samples are added to the main replay buffer, and the sampling process is updated with the latest parameters from the learning process.

4 Experiments

Datasets. We use the MD17 dataset, which contains conformations for ethanol, malondialdehyde, and uracil Chmiela et al. (2017), generated via molecular dynamics at the DFT level of theory using the def2-SVP Gaussian-Type Orbital (GTO) basis set and the PBE exchange-correlation functional Perdew et al. (1996). We use the standard train/validation/test splits from Schütt et al. (2019). To explore data scarcity, we consider a reduced data scenarios using only 10% of the full dataset, which we run our self-refining method on top of these subsets. In the data-rich setting, we have full access to the conformations from the MD17 dataset and generate additional samples using our self-refining method.

Metrics. We follow the standard metrics introduced in prior work Schütt et al. (2019). Specifically, we report the mean absolute error (MAE) between the Hamiltonian matrix derived from the model’s predicted coefficients and the reference DFT-computed Hamiltonian. We also measure the MAE of the orbital energies ϵ and four molecular properties: the highest occupied molecular orbital ϵ_{HOMO} , the lowest unoccupied molecular orbital ϵ_{LUMO} , the energy gap ϵ_{Δ} , and the total energy E .

Baselines. We compare our self-refining approach to models that learn the energy via the implicit DFT loss on pre-collected conformations. All experiments are conducted on conformations from the MD17 dataset, using the 6-31G GTO basis set for ethanol and malondialdehyde, and the STO-3g GTO basis set for uracil. For all systems, we use the PBE exchange-correlation functional. Since this basis choice differs from the def2-SVP GTO basis set originally used to generate MD17, we compute ground-truth properties through the PySCF library Sun et al. (2018) with the corresponding basis and exchange-correlation functionals, then evaluate using the metrics described above.

4.1 Improving Performance

We demonstrate that self-refining training improves performance both in the data-scarce scenario and on the out-of-distribution samples.

Data-Scarce Scenario. Data scarcity is a common challenge in many scientific domains where few or no conformations and their corresponding DFT labels are available. In these low-data regimes, data-hungry methods often perform poorly. To demonstrate the effectiveness of our self-refining approach, we evaluate performance under various levels of data availability – 0.1 %, 1%, 10%, 100%

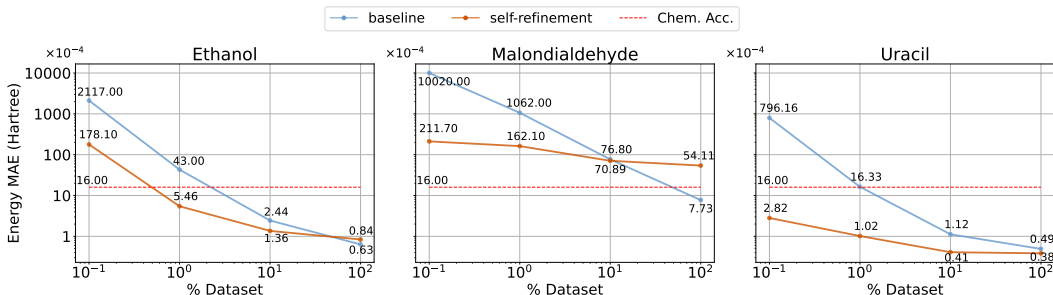


Figure 2: Energy prediction error (MAE in $\times 10^{-4}$ Hartree) of the baseline and self-refining models across varying dataset sizes for three molecules. The self-refining approach consistently improves accuracy, especially in low-data regimes, often achieving chemical accuracy (red dashed line) with significantly fewer training points.

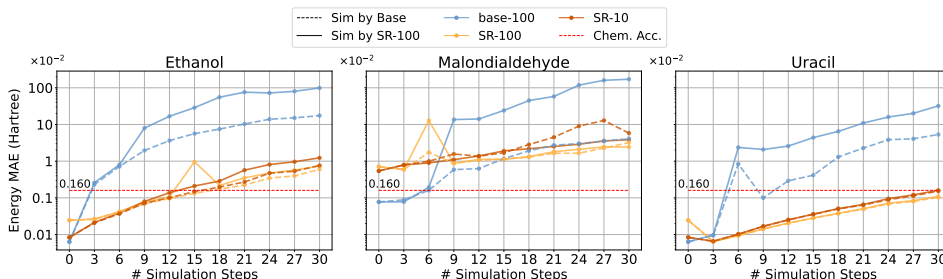


Figure 3: Generalization of baseline and self-refining models evaluated on samples generated from simulation. We report the energy MAE ($\times 10^{-2}$ Hartree) over 30 simulation steps for models trained on 10% or 100% of the data, with samples propagated by either the baseline model (dashed) or self-refining model (solid) trained on 100% of data. The self-refining approach consistently yields lower errors and maintains accuracy further into the simulation, demonstrating improved robustness to out-of-distribution samples. The red dashed line marks the chemical accuracy threshold (0.16×10^{-2} Hartree).

– corresponding to 25, 250, 2500, 25000 conformations, respectively, for ethanol, malondialdehyde, and uracil. We compare the baseline model trained using the implicit DFT loss solely on the available data against the same model augmented by the self-refining procedure. As shown in Table 1 and Fig. 2, self-refinement yields performance gains in low-data settings, often matching the performance of the baseline model trained on the full dataset using only 10% of the data. These results highlight the ability of our framework to mitigate data scarcity, suggesting a viable solution for learning in data-limited settings.

Out-of-Distribution Scenario. To assess the generalization ability of our electronic state model beyond the training distribution, we evaluate the prediction accuracy of energy across simulation trajectories. Specifically, we consider two types of simulations: those generated by the baseline model and those generated by the self-refining model trained on 100% of the data. At every 3 simulation steps, we compute the energy MAE for the baseline, SR-10%, and SR-100% models. As shown in Section 4.1, the self-refined models exhibit significantly improved robustness, maintaining low error even as the trajectory progresses further from the training distribution. In contrast, the baseline model quickly deteriorates, producing inaccurate energy estimates once the samples drift outside the support of the training set. This demonstrates that incorporating self-refinement during training leads to more reliable predictions on out-of-distribution samples.

4.2 Efficiency from Simultaneous Training and Generation

The self-refining method significantly reduces the overall time spent on (1) collecting conformations, (2) labeling with DFT, and (3) training the model as shown in Fig. 4, as these steps are performed simultaneously. A key benefit is that iterative DFT minimization need not be run to convergence for each conformation. Instead, amortizing the optimization by training through the implicit DFT loss, we predict ground-state solutions on the fly during inference and sample new data from an imperfect, evolving energy model. This capability removes the barrier of requiring fully annotated data as a prerequisite for training robust, generalizable models. Details on how the runtimes were evaluated can be found in Appendix C.4.

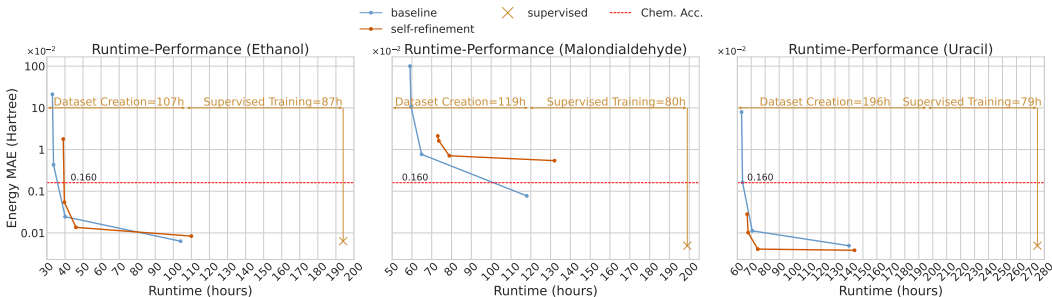


Figure 4: Runtime vs. performance comparison for baseline, self-refining, and supervised models on Ethanol and Uracil. We report the energy MAE ($\times 10^{-2}$ Hartree) as a function of total runtime, including data generation, labeling, and training. The self-refining method approaches the performance of supervised models with significantly lower runtime. Orange bars indicate time spent on dataset creation and supervised training for the QHNet model. The red dashed line marks the chemical accuracy threshold.

5 Related Work

Direct Energy Minimization in DFT. Our work significantly relies on the direct energy minimization literature (Head-Gordon and Pople, 1988; Kasim et al., 2022), which suggests finding the ground state as the state minimizing the energy of the system unlike SCF. This approach together with the frameworks for automatic differentiation (Bradbury et al., 2018; Paszke et al., 2019) unlocked new family of algorithms that allows for designing stable and efficient DFT solvers (Weber et al., 2008; Yoshikawa and Sumita, 2022; Helal and Fitzgibbon, 2024). In our work, direct energy minimization naturally appears as minimization of the variational upper bound Section 3.2.

Amortized DFT. Deep learning allows for training models that directly predict the optimal electronic state or energy bypassing expensive DFT solvers for every new input geometry. This can be achieved either by learning the regression models for labeled data (Ramakrishnan et al., 2014; Schütt et al., 2018; Falletta et al., 2024), by introducing the self-consistency loss analogous to SCF (Zhang et al., 2024a), or, analogous to our method, by directly minimizing the energy of the predicted electronic state (Mathiasen et al., 2024; Li et al., 2024). However, all the previous methods consider training on a fixed dataset of conformations and do not reuse the parameterized energy model for generating new ones.

Data-Augmentation. From the Machine Learning perspective our method can be considered as data-augmentation technique (Perez and Wang, 2017) or adversarial training (Goodfellow et al., 2014b). The important difference here is that our method relies neither on domain symmetry (which can be additionally utilized) nor on the existence of adversarial examples. On contrary, the Langevin dynamics that we use for generating new samples at the sampling step (see Section 3.3) simulates the overdamped molecular dynamics; thus, we directly optimize the performance of our model on one of the downstream tasks.

6 Conclusion

In this paper, we provide a unified perspective on learning the energy model (amortized DFT) and generating conformations. The validity of our approach is established by a variational upper bound on the KL-divergence between the distribution of conformations and the ground truth Boltzmann density. Furthermore, we demonstrate that this perspective is practical and improves performance of the model across multiple systems for different available datasets.

We believe that our approach serves as an important stepping stone towards scalable and efficient *ab initio* modeling of molecular systems that relies solely on the knowledge of underlying physical laws. In particular, combining the proposed algorithm with recent advances in learnable samplers Noé et al. (2019); Akhoun-Sadegh et al. (2024), one can simultaneously train both the energy model and the generative model that samples from the corresponding Boltzmann density. Furthermore, our approach is agnostic to the implementation of the energy functional, which makes it compatible with other perspective avenues for improvement of DFT. For instance, it can be combined with stochastic estimates of the quadrature (Li et al., 2023) or orbital-free DFT calculations (Zhang et al., 2024b; de Camargo et al., 2024).

7 Acknowledgments

The research was enabled in part by computational resources provided by Mila Quebec AI Institute (<https://mila.quebec>) and Valence Labs / Recursion. KN was supported by IVADO and Institut Courtois.

References

- Akhound-Sadegh, T., Rector-Brooks, J., Bose, A. J., Mittal, S., Lemos, P., Liu, C.-H., Sendera, M., Ravanbakhsh, S., Gidel, G., Bengio, Y., Malkin, N., and Tong, A. (2024). Iterated Denoising Energy Matching for Sampling from Boltzmann Densities. *arXiv:2402.06121 [cs, stat]*.
- Ambrosio, L. and Savaré, G. (2007). Gradient Flows of Probability Measures. In *Handbook of Differential Equations: Evolutionary Equations*, volume 3, pages 1–136. Elsevier.
- Beaini, D., Huang, S., Cunha, J. A., Li, Z., Moisescu-Pareja, G., Dymov, O., Maddrell-Mander, S., McLean, C., Wenkel, F., Müller, L., Mohamud, J. H., Parviz, A., Craig, M., Koziarski, M., Lu, J., Zhu, Z., Gabellini, C., Klaser, K., Dean, J., Wognum, C., Sypetkowski, M., Rabusseau, G., Rabbany, R., Tang, J., Morris, C., Koutis, I., Ravanelli, M., Wolf, G., Tossou, P., Mary, H., Bois, T., Fitzgibbon, A., Banaszewski, B., Martin, C., and Masters, D. (2023). Towards Foundational Models for Molecular Learning on Large-Scale Multi-Task Datasets. *arXiv:2310.04292 [cs]*.
- Bradbury, J., Frostig, R., Hawkins, P., Johnson, M. J., Leary, C., Maclaurin, D., Necula, G., Paszke, A., VanderPlas, J., Wanderman-Milne, S., and Zhang, Q. (2018). JAX: composable transformations of Python+NumPy programs.
- Chmiela, S., Tkatchenko, A., Sauceda, H. E., Poltavsky, I., Schütt, K. T., and Müller, K.-R. (2017). Machine learning of accurate energy-conserving molecular force fields. *Science Advances*, 3(5):e1603015. Publisher: American Association for the Advancement of Science.
- de Camargo, A., Chen, R. T., and Vargas-Hernández, R. A. (2024). Leveraging normalizing flows for orbital-free density functional theory. *Machine Learning: Science and Technology*, 5(3):035061.
- Deng, J., Dong, W., Socher, R., Li, L.-J., Li, K., and Fei-Fei, L. (2009). ImageNet: A large-scale hierarchical image database. In *2009 IEEE Conference on Computer Vision and Pattern Recognition*, pages 248–255. ISSN: 1063-6919.
- Falletta, S., Cepellotti, A., Johansson, A., Tan, C. W., Musaelian, A., Owen, C. J., and Kozinsky, B. (2024). Unified differentiable learning of electric response.
- Goodfellow, I. J., Pouget-Abadie, J., Mirza, M., Xu, B., Warde-Farley, D., Ozair, S., Courville, A., and Bengio, Y. (2014a). Generative adversarial nets. *Advances in neural information processing systems*, 27.
- Goodfellow, I. J., Shlens, J., and Szegedy, C. (2014b). Explaining and harnessing adversarial examples. *arXiv preprint arXiv:1412.6572*.
- Hassan, M., Shenoy, N., Lee, J., Stark, H., Thaler, S., and Beaini, D. (2024). ET-Flow: Equivariant Flow-Matching for Molecular Conformer Generation. *arXiv:2410.22388 [q-bio]*.
- Head-Gordon, M. and Pople, J. A. (1988). Optimization of wave function and geometry in the finite basis Hartree-Fock method. *The Journal of Physical Chemistry*, 92(11):3063–3069. Publisher: American Chemical Society.
- Hehre, W. J., Stewart, R. F., and Pople, J. A. (1969). Self-Consistent Molecular-Orbital Methods. I. Use of Gaussian Expansions of Slater-Type Atomic Orbitals. *The Journal of Chemical Physics*, 51(6):2657–2664.
- Helal, H. and Fitzgibbon, A. (2024). MESS: Modern Electronic Structure Simulations. *arXiv:2406.03121 [cs]*.
- Hohenberg, P. and Kohn, W. (1964a). Inhomogeneous Electron Gas. *Physical Review*, 136(3B):B864–B871. Publisher: American Physical Society.

- Hohenberg, P. and Kohn, W. (1964b). Inhomogeneous electron gas. *Physical review*, 136(3B):B864.
- Kasim, M. F., Lehtola, S., and Vinko, S. M. (2022). DQC: a Python program package for Differentiable Quantum Chemistry. *The Journal of Chemical Physics*, 156(8):084801. arXiv:2110.11678 [physics].
- Keith, J. A., Vassilev-Galindo, V., Cheng, B., Chmiela, S., Gastegger, M., Müller, K.-R., and Tkatchenko, A. (2021). Combining Machine Learning and Computational Chemistry for Predictive Insights Into Chemical Systems. *Chemical Reviews*, 121(16):9816–9872. Publisher: American Chemical Society.
- Kohn, W. and Sham, L. J. (1965a). Self-Consistent Equations Including Exchange and Correlation Effects. *Physical Review*, 140(4A):A1133–A1138. Publisher: American Physical Society.
- Kohn, W. and Sham, L. J. (1965b). Self-consistent equations including exchange and correlation effects. *Phys. Rev.*, 140:A1133–A1138.
- Leimkuhler, B. and Matthews, C. (2015). *Molecular Dynamics: With Deterministic and Stochastic Numerical Methods*. Springer.
- Li, T., Lin, M., Hu, Z., Zheng, K., Vignale, G., Kawaguchi, K., Neto, A. H. C., Novoselov, K. S., and Yan, S. (2023). D4FT: A Deep Learning Approach to Kohn-Sham Density Functional Theory. arXiv:2303.00399 [cs].
- Li, Y., Tang, Z., Chen, Z., Sun, M., Zhao, B., Li, H., Tao, H., Yuan, Z., Duan, W., and Xu, Y. (2024). Neural-network Density Functional Theory Based on Variational Energy Minimization. *Physical Review Letters*, 133(7):076401. arXiv:2403.11287 [physics].
- Mathiasen, A., Helal, H., Balanca, P., Krzywaniak, A., Parviz, A., Hvilshøj, F., Banaszewski, B., Luschi, C., and Fitzgibbon, A. W. (2024). Reducing the Cost of Quantum Chemical Data By Backpropagating Through Density Functional Theory. arXiv:2402.04030 [cs].
- Nakata, M. and Shimazaki, T. (2017). PubChemQC Project: A Large-Scale First-Principles Electronic Structure Database for Data-Driven Chemistry. *Journal of Chemical Information and Modeling*, 57(6):1300–1308.
- Noé, F., Olsson, S., Köhler, J., and Wu, H. (2019). Boltzmann Generators – Sampling Equilibrium States of Many-Body Systems with Deep Learning. arXiv:1812.01729 [stat].
- Parr, R. G. (1980). Density Functional Theory of Atoms and Molecules. In Fukui, K. and Pullman, B., editors, *Horizons of Quantum Chemistry*, pages 5–15, Dordrecht. Springer Netherlands.
- Paszke, A., Gross, S., Massa, F., Lerer, A., Bradbury, J., Chanan, G., Killeen, T., Lin, Z., Gimelshein, N., Antiga, L., Desmaison, A., Köpf, A., Yang, E., DeVito, Z., Raison, M., Tejani, A., Chilamkurthy, S., Steiner, B., Fang, L., Bai, J., and Chintala, S. (2019). PyTorch: An Imperative Style, High-Performance Deep Learning Library. arXiv:1912.01703 [cs].
- Payne, M. C., Teter, M. P., Allan, D. C., Arias, T. A., and Joannopoulos, J. D. (1992). Iterative minimization techniques for ab initio total-energy calculations: molecular dynamics and conjugate gradients. *Reviews of Modern Physics*, 64(4):1045–1097. Publisher: American Physical Society.
- Perdew, J. P., Burke, K., and Ernzerhof, M. (1996). Generalized Gradient Approximation Made Simple. *Physical Review Letters*, 77(18):3865–3868. Publisher: American Physical Society.
- Perez, L. and Wang, J. (2017). The effectiveness of data augmentation in image classification using deep learning. *arXiv preprint arXiv:1712.04621*.
- Pribram-Jones, A., Gross, D. A., and Burke, K. (2015). DFT: A Theory Full of Holes? *Annual Review of Physical Chemistry*, 66(Volume 66, 2015):283–304. Publisher: Annual Reviews.
- Ramakrishnan, R., Dral, P. O., Rupp, M., and von Lilienfeld, O. A. (2014). Quantum chemistry structures and properties of 134 kilo molecules. *Scientific Data*, 1(1):140022. Publisher: Nature Publishing Group.

- Roothaan, C. C. J. (1951). New Developments in Molecular Orbital Theory. *Reviews of Modern Physics*, 23(2):69–89. Publisher: American Physical Society.
- Schütt, K. T., Gastegger, M., Tkatchenko, A., Müller, K.-R., and Maurer, R. J. (2019). Unifying machine learning and quantum chemistry – a deep neural network for molecular wavefunctions. arXiv:1906.10033 [physics].
- Schütt, K. T., Sauceda, H. E., Kindermans, P.-J., Tkatchenko, A., and Müller, K.-R. (2018). SchNet - A deep learning architecture for molecules and materials. *The Journal of Chemical Physics*, 148(24):241722.
- Sun, Q., Berkelbach, T. C., Blunt, N. S., Booth, G. H., Guo, S., Li, Z., Liu, J., McClain, J. D., Sayfutyarova, E. R., Sharma, S., Wouters, S., and Chan, G. K.-L. (2018). PySCF: the Python-based simulations of chemistry framework. *WIREs Computational Molecular Science*, 8(1):e1340. [_eprint: https://onlinelibrary.wiley.com/doi/pdf/10.1002/wcms.1340](https://onlinelibrary.wiley.com/doi/pdf/10.1002/wcms.1340).
- Thölke, P. and Fabritiis, G. D. (2022). TorchMD-NET: Equivariant Transformers for Neural Network based Molecular Potentials. arXiv:2202.02541 [cs].
- Unke, O. T., Chmiela, S., Sauceda, H. E., Gastegger, M., Poltavsky, I., Schütt, K. T., Tkatchenko, A., and Müller, K.-R. (2021). Machine Learning Force Fields. *Chemical Reviews*, 121(16):10142–10186. Publisher: American Chemical Society.
- Weber, V., VandeVondele, J., Hutter, J., and Niklasson, A. M. N. (2008). Direct energy functional minimization under orthogonality constraints. *The Journal of Chemical Physics*, 128(8):084113.
- Yoshikawa, N. and Sumita, M. (2022). Automatic Differentiation for the Direct Minimization Approach to the Hartree-Fock Method. *The Journal of Physical Chemistry A*, 126(45):8487–8493. arXiv:2203.04441 [physics].
- Yu, H., Xu, Z., Qian, X., Qian, X., and Ji, S. (2023). Efficient and Equivariant Graph Networks for Predicting Quantum Hamiltonian. arXiv:2306.04922 [cs].
- Zhang, H., Liu, C., Wang, Z., Wei, X., Liu, S., Zheng, N., Shao, B., and Liu, T.-Y. (2024a). Self-Consistency Training for Density-Functional-Theory Hamiltonian Prediction. arXiv:2403.09560 [cs].
- Zhang, H., Liu, S., You, J., Liu, C., Zheng, S., Lu, Z., Wang, T., Zheng, N., and Shao, B. (2024b). Overcoming the barrier of orbital-free density functional theory for molecular systems using deep learning. *Nature Computational Science*, 4(3):210–223.

A Proofs

A.1 Proof of Proposition 1

Proposition 1. [Variational Energy Bound] *For any density $q(R)$, the KL-divergence between $q(R)$ and the ground-state Boltzmann distribution $p^*(R) \propto \exp(-E(R, f^*(R)))$ admits the following variational upper bound*

$$D_{\text{KL}}(q, p^*) \leq \underbrace{\mathbb{E}_{q(R)} \log q(R) + \mathbb{E}_{q(R)} E(R, f_\theta(R))}_{:=\Phi[q, f_\theta]} + \log Z^*, \quad (10)$$

where f_θ is a parametric approximation of f^* , which satisfies $f_\theta(R)^\dagger S(R) f_\theta(R) = \mathbb{1}$. For any $q(R)$, the bound becomes tight when $f_\theta(R) = f^*(R)$.

Proof. We denote the solution f^* to the optimization problem in Eq. (7) as

$$f^*(R) = \arg \min_{C: C^\dagger S(R) C = \mathbb{1}} E(R, C). \quad (16)$$

We define $f_\theta(R)$ as a parametric model for which we guarantee

$$f_\theta(R)^\dagger S(R) f_\theta(R) = \mathbb{1}, \quad (17)$$

which can be done using the QR-decomposition (see Section 3.2 for the explicit construction). Then, for this parametric family, we have

$$E(R, f^*(R)) \leq E(R, f_\theta(R)), \quad \forall \theta, \quad (18)$$

$$-E(R, f^*(R)) \pm \log Z^* \geq -E(R, f_\theta(R)) \pm \log Z, \quad (19)$$

$$\log p^*(R) + \log Z^* \geq \log p(R) + \log Z, \quad (20)$$

$$\mathbb{E}_{q(R)} \log p^*(R) + \log Z^* \geq \mathbb{E}_{q(R)} \log p(R) + \log Z, \quad (21)$$

$$\log \frac{Z^*}{Z} \geq \mathbb{E}_{q(R)} \log \frac{p(R)}{p^*(R)}, \quad (22)$$

where $p(R) \propto \exp(-E(R, f_\theta(R)))$ is the Boltzmann density of the parametrized energy model and $Z = \int dR \exp(-E(R, f_\theta(R)))$ is its normalization constant.

Consider the minimization of the KL-divergence between the distribution of samples q and the target Boltzmann distribution p^* , then we have the following estimate

$$D_{\text{KL}}(q, p^*) := \mathbb{E}_{q(R)} \log \frac{q(R)}{p^*(R)} = \mathbb{E}_{q(R)} \log \frac{q(R)}{p(R)} + \mathbb{E}_{q(R)} \log \frac{p(R)}{p^*(R)}, \quad \forall p(R) \quad (23)$$

$$\leq \mathbb{E}_{q(R)} \log \frac{q(R)}{p(R)} + \log \frac{Z^*}{Z} = D_{\text{KL}}(q, p) + \log \frac{Z^*}{Z}, \quad (24)$$

which holds for any $p(R)$, but choosing $p(R) = Z^{-1} \exp(-E(R, f_\theta(R)))$, we get

$$D_{\text{KL}}(q, p) + \log \frac{Z^*}{Z} = \mathbb{E}_{q(R)} \log q(R) + \mathbb{E}_{q(R)} (-\log p(R) - \log Z) + \log Z^* \quad (25)$$

$$= \underbrace{\mathbb{E}_{q(R)} \log q(R) + \mathbb{E}_{q(R)} E(R, f_\theta(R))}_{\Phi[q, f_\theta]} + \log Z^*. \quad (26)$$

Thus, we have

$$D_{\text{KL}}(q, p^*) \leq \underbrace{\mathbb{E}_{q(R)} \log q(R) + \mathbb{E}_{q(R)} E(R, f_\theta(R))}_{\Phi[q, f_\theta]} + \log Z^*. \quad (27)$$

Note that taking $f_\theta(R) = f^*(R)$, the upper bound becomes

$$D_{\text{KL}}(q, p^*) \leq \mathbb{E}_{q(R)} \log q(R) + \mathbb{E}_{q(R)} E(R, f_\theta(R)) + \log Z^* \quad (28)$$

$$= \mathbb{E}_{q(R)} \log q(R) - [\mathbb{E}_{q(R)} (-E(R, f^*(R))) - \log Z^*] = D_{\text{KL}}(q, p^*). \quad (29)$$

Hence, for any $q(R)$, we can find $f_\theta = f^*$ for which the bound becomes tight. \square

A.2 Proof of Corollary 2

Corollary 2. [Sampling] For any electronic state model $f_\theta(R)$, the optimum of the upper bound $\Phi[q, f_\theta]$ w.r.t. the density $q(R)$ is the Boltzmann distribution defined by the model $f_\theta(R)$, i.e.

$$q^*(R) = \arg \min_q \Phi[q, f_\theta] = \frac{1}{Z_\theta} \exp(-E(R, f_\theta(R))). \quad (13)$$

Proof. Recall that, for the functional $F[q]$, the functional derivative is defined through the infinitesimal change of the functional along the direction h as follows

$$F[q + h] = F[q] + \int dx h(x) \underbrace{\frac{\delta F[q]}{\delta q}}_{\text{derivative}}(x) + o(\|h\|), \quad (30)$$

which can be found as

$$\left. \frac{\partial F[q + \varepsilon h]}{\partial \varepsilon} \right|_{\varepsilon=0} = \int dx h(x) \frac{\delta F[q]}{\delta q}(x). \quad (31)$$

Now, consider the functional

$$\Phi[q, f_\theta] = \mathbb{E}_{q(R)}[\log q(R) + E(R, f_\theta(R))], \quad \text{subject to} \quad \int dR q(R) = 1. \quad (32)$$

Its Lagrangian is

$$\mathcal{L}[q] = \mathbb{E}_{q(R)} \log q(R) + \mathbb{E}_{q(R)} E(R, f_\theta(R)) + \lambda \left(\int dR q(R) - 1 \right), \quad (33)$$

and its functional derivative is

$$\begin{aligned} \left. \frac{\partial \mathcal{L}[q + \varepsilon h]}{\partial \varepsilon} \right|_{\varepsilon=0} &= \left. \frac{\partial}{\partial \varepsilon} \int dR (q(R) + \varepsilon h(R)) [\log(q(R) + \varepsilon h(R)) + E(R, f_\theta(R)) + \lambda] \right|_{\varepsilon=0} \\ &= \int dR h(R) \underbrace{[\log q(R) + E(R, f_\theta(R)) + \lambda]}_{\delta \mathcal{L} / \delta q} + \int dR q(R) \frac{h(R)}{q(R)} \overset{0}{\rightarrow}. \end{aligned} \quad (34)$$

Thus, for the optimal q , we have

$$\frac{\delta \mathcal{L}}{\delta q} = 0 \quad (35)$$

$$\log q(R) + E(R, f_\theta(R)) = -\lambda \quad (36)$$

$$q(R) = \frac{1}{Z_\theta} \exp(-E(R, f_\theta(R))), \quad Z_\theta = \int dR \exp(-E(R, f_\theta(R))), \quad (37)$$

where the last expression we get from the normalization condition. \square

A.3 Proof of Proposition 2

Proposition 2. [Wasserstein Gradient] For the functional $\Phi[q, f_\theta]$ defined in Proposition 1, the gradient descent w.r.t. $q(R)$ corresponds to the following PDE

$$\frac{\partial q_t(R)}{\partial t} = -\langle \nabla_R, q_t(R) (-\nabla_R E(R, f_\theta(R))) \rangle + \Delta_R q_t(R), \quad (14)$$

which can be efficiently simulated via the following Stochastic Differential Equation (SDE)

$$dR_t = -\nabla_R E(R_t, f_\theta(R_t)) dt + \sqrt{2} dW_t, \quad (15)$$

where W_t is the standard Wiener process.

Proof. Recall that the Wasserstein gradient can be derived as the vector field $v_t(x)$ that maximizes the change of the functional $F[q_t]$

$$\frac{d}{dt}F[q_t] = \int dx \frac{\partial q_t(x)}{\partial t} \frac{\delta F[q_t]}{\delta q_t}, \quad (38)$$

when the density $q_t(x)$ changes according to the continuity equation

$$\frac{\partial q_t(x)}{\partial t} = -\langle \nabla_x, q_t(x) v_t(x) \rangle. \quad (39)$$

Thus, we have

$$\frac{d}{dt}F[q_t] = \int dx q_t(x) \left\langle v_t(x), \nabla_x \frac{\delta F[q_t]}{\delta q_t} \right\rangle \implies v_t(x) = \nabla_x \frac{\delta F[q_t]}{\delta q_t}, \quad (40)$$

where $\delta F[q_t]/\delta q_t$ is the functional derivative of $F[q_t]$.

Applying this reasoning for the functional $\Phi[q_t, f_\theta]$, we first have to find the functional derivative. That is, for the functional

$$\Phi[q, f_\theta] = \mathbb{E}_{q(R)}[\log q(R) + E(R, f_\theta(R))], \quad (41)$$

its functional derivative is

$$\begin{aligned} \left. \frac{\partial \Phi[q, f_\theta][q + \varepsilon h]}{\partial \varepsilon} \right|_{\varepsilon=0} &= \frac{\partial}{\partial \varepsilon} \int dR (q(R) + \varepsilon h(R)) [\log(q(R) + \varepsilon h(R)) + E(R, f_\theta(R))] \Big|_{\varepsilon=0} \\ &= \int dR h(R) \underbrace{[\log q(R) + E(R, f_\theta(R))]}_{\delta \Phi[q, f_\theta]/\delta q} + \cancel{\int dR q(R) \frac{h(R)}{q(R)}} \rightarrow 0 \end{aligned} \quad (42)$$

$$\frac{\delta \Phi[q, f_\theta]}{\delta q} = \log q(R) + E(R, f_\theta(R)). \quad (43)$$

Thus, the PDE corresponding to the negative gradient flow is

$$\frac{\partial q_t(R)}{\partial t} = - \left\langle \nabla_R, q_t(R) \left(-\nabla_R \frac{\delta \Phi[q_t, f_\theta]}{\delta q_t} \right) \right\rangle \quad (44)$$

$$= - \langle \nabla_R, q_t(R) (-\nabla_R \log q(R) - \nabla_R E(R, f_\theta(R))) \rangle \quad (45)$$

$$= - \langle \nabla_R, q_t(R) (-\nabla_R E(R, f_\theta(R))) \rangle + \Delta q(R). \quad (46)$$

This PDE is the Fokker-Planck equation, which can be efficiently simulated using the following SDE

$$dR_t = -\nabla_R E(R, f_\theta(R)) dt + \sqrt{2} dW_t, \quad (47)$$

where W_t is the standard Wiener process. \square

B Architecture Details

We use a hybrid transformer architecture composed of an SO(3)-equivariant transformer backbone (Thölke and Fabritiis, 2022; Hassan et al., 2024), and a transformer with quantum-biased attention for coefficient prediction (Mathiasen et al., 2024). The backbone operates on a fully-connected molecular graph, where node features encode atomic types and 3D positions, and edge features represent pairwise distances. It produces atomic representations which are combined with orbital-specific embeddings and passed to the transformer-based coefficient network to predict the molecular orbital coefficients.

Orbital tokenization and embedding. To incorporate orbital-specific information into the coefficient prediction network, we define a fixed mapping from atomic orbital types (e.g., 1s, 2px, 3dxy) to unique integer tokens. For each molecule, we extract atomic orbital (AO) labels from the pySCF, tokenize the orbital type using this mapping, and associate each orbital with the index of its parent atom. This allows us to extend atom-level features to the orbital level within the coefficient network.

Coefficient network. The coefficient network operates on fused atomic and orbital representations, where the atomic embeddings are indexed by orbital indices to ensure that each orbital inherits the

representation from its associated atom. The orbital tokens T_{orb} are then embedded using a learned embedding layer, and the resulting embeddings are added to the atomic representations:

$$\mathbf{x}_{\text{orb}} = \mathbf{x}_{\text{atom}}[\text{index}] + \text{Embed}(T_{\text{orb}}). \quad (48)$$

The fused representations are processed by a stack of multi-head attention blocks that incorporate quantum-based biases, including the core Hamiltonian matrix H_{core} (comprising kinetic and nuclear terms), the Coulomb-exchange difference $(J - K/2)$, and the term $S(R)H_{\text{core}}S(R)^\top$, following (Mathiasen et al., 2024). The final term is the transformation of the core Hamiltonian into an orthonormal basis, where $S(R) = U\Lambda^{-\frac{1}{2}}U^\top$ is obtained via symmetric orthonormalization of the overlap matrix.

The final output of the transformer is projected and used to construct the un-orthonormalized coefficient matrix

$$Z = \frac{QK^\top}{\sqrt{d_K}} \quad (49)$$

where Q and K are the query and key matrices, and d_K is the dimensionality of the keys. The orbital coefficients C are then obtained by orthonormalizing Z using the reparameterization described in Eq. (11). These coefficients are used to compute the total energy $E(R, C)$ for the given configuration R with Hamiltonian H , and the model is trained by minimizing this energy with respect to the network parameters θ . This design enables the network to distinguish among different orbitals on the same atom, and to generalize across molecules by learning shared embeddings for common orbital types. Model hyperparameters are provided in Table 3.

C Experimental Settings

C.1 Dataset Details

Table 2 summarizes the relevant statistics and choice of basis set for each molecular system in the MD17 dataset.

Table 2: Statistics for MD17 dataset and experimental setting choices.

Molecule	Train (100%)	Validation	Test	# Atoms	# Orbitals	Basis Set
Ethanol	25,000	500	4500	9	39	6-31G
Malondialdehyde	25,000	500	1478	9	53	6-31G
Uracil	25,000	500	4500	12	41	STO-3G

C.2 Training Details and Hyperparameters

Training Configuration. For all molecular systems, we explore the various configurations detailed in Table 4. We use the AdamW Optimizer with a weight decay of 10^{-6} , and apply cosine annealing to the learning rate, decreasing it from a maximum of $3 \cdot 10^{-4}$ to a minimum 10^{-6} over the course of training. Model checkpoints are selected based on the lowest validation energy computed on MD17 conformations for each molecular system.

Replay Buffer. The replay buffer stores previously generated samples, which are uniformly sampled during the training of the ES model. To prevent overfitting, we maintain a buffer size of up to 2048 samples. This buffer size also promotes samples diversity, as the stored samples are used to initialize Langevin dynamics. Once the buffer reaches capacity, it operates in a first-in-first-out (FIFO) manner, discarding the oldest samples as new ones are added.

C.3 Resources

For all settings, we run our experiments on a cluster using one Nvidia H100 GPU for the baseline experiments, and two H100 GPUs for the self-refining method where one GPU is used to train the electronic state model, and the other GPU is used to sample from the energy of the model.

Table 3: Hyperparameters for the transformer-based electronic structure model.

Hyper-parameter	Setting
num_layers	6
num_coef_layers	6
hidden_channels	256
num_heads	8
neighbor_embedding	True
node_attr_dim	1
edge_attr_dim	1
reduce_op	True
activation	SiLU
attn_activation	SiLU
skip_connection	True
# param	8.4M

Table 4: Experimental settings for training the electronic state model.

Setting	Dataset Size	Batch Size	# Iterations	# Pretrain Iterations
$\mathcal{D}_{100\%}$	25,000	8	200K	0
$\mathcal{D}_{0.1\%}$ + SR	25	8	200K	10K
$\mathcal{D}_{1\%}$ + SR	250	8	200K	10K
$\mathcal{D}_{10\%}$ + SR	2,500	8	200K	10K
$\mathcal{D}_{100\%}$ + SR	25,000	8	200K	10K

C.4 Runtime Analysis

The runtime analysis consists of three main components: (1) the time required to perform molecular dynamics (MD) simulations, (2) the time to label conformations with DFT-computed energies, and (3) the time to train the model.

To estimate the runtime for MD simulations, we follow the settings provided in (Schütt et al., 2019). We run simulations for 5ps to measure the wall-clock time and extrapolate to a total simulation length of 200ps. This estimate accounts only for integration time and does not include the cost of computing energies and forces at each step, which may vary depending on the force field or simulator used.

For DFT labeling, we use PySCF to compute total energies for a batch of 100 conformations and extrapolate the runtime to a full dataset of 25,000 conformations.

Model training time is evaluated under two scenarios. In the first, we perform supervised training using QHNet on the full pre-collected dataset. The total runtime includes both the time to generate the complete dataset (MD + DFT labeling) and the time to train the model. In the second scenario, we use self-refinement, starting from only 10% of the pre-collected dataset. The total runtime in this case includes the time to generate the initial 10% of conformations and the training time for self-refinement. Importantly, this setting eliminates the need for costly DFT energy labels, as the model is optimized directly using energy evaluations rather than by regressing to ground-truth labels.

In both scenarios, training runtimes are measured using an NVIDIA A100 GPU. A comparison of the runtimes across these settings is presented in Fig. 4.